Au Nanorod Helical Superstructures with Designed Chirality

Xiang Lan,[†] Xuxing Lu,[†] Chenqi Shen,[†] Yonggang Ke,[‡] Weihai Ni,[†] and Qiangbin Wang*,[†]

[†]Key Laboratory of Nano-Bio Interface, Division of Nanobiomedicine and i-Lab, CAS Center for Excellence in Brain Science, Suzhou Institute of Nano-Tech and Nano-Bionics, Chinese Academy of Sciences, Suzhou, 215123 China

[‡]Wallace H. Coulter Department of Biomedical Engineering, Georgia Institute of Technology and Emory University, Atlanta, Georgia 30322, United States

S *Supporting Information*

ABSTRACT: A great challenge for nanotechnology is to controllably organize anisotropic nanomaterials into well-defined three-dimensional superstructures with customized properties. Here we successfully constructed anisotropic Au nanorod (AuNR) helical superstructures (helices) with tailored chirality in a programmable manner. By designing the 'X' pattern of the arrangement of DNA capturing strands (15nt) on both sides of a two-dimensional DNA origami template, AuNRs functionalized with the complementary DNA sequences were positioned on the origami and were assembled into AuNR helices with the origami intercalated between neighboring AuNRs. Left-handed (LH) and right-handed (RH) AuNR helices were conveniently accomplished by solely tuning the mirrored-symmetric 'X' patterns of capturing strands on the origami. The inter-rod distance was precisely defined as 14 nm and inter-rod angle as 45°, thus a full helix contains 9 AuNRs with its length up to about 220 nm. By changing the AuNR/origami molar ratio in the assembly system, the average number of AuNR in the helices was tuned from 2 to 4 and 9. Intense chiroptical activities arose from the longest AuNR helices with a maximum anisotropy factor of ~0.02, which is highly comparable to the reported macroscopic AuNR assemblies. We expect that our strategy of origami templated assembly of anisotropic chiral superstructures would inspire the bottom-up fabrication of optically active nanostructures and shed light on a variety of applications, such as chiral fluids, chiral signal amplification, and fluorescence combined chiral spectroscopy.
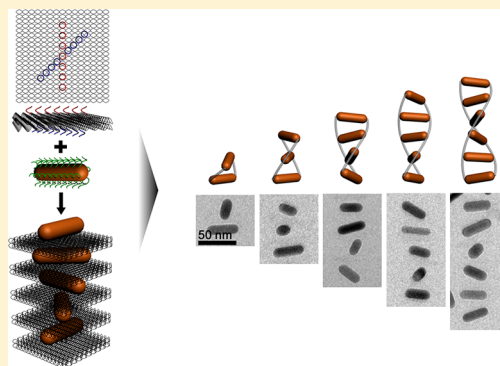
Chirality exists extensively in nature, spanning from small molecules such as L-amino acids and D-sugars to macroscale objects such as plant vines and the human body. Manufacture of chiral materials and exploitation of the optical activities in plasmonics, nanophotonics, and ultrasensitive sensing are the hot topics of current research.[1−7] Electron beam lithography has been used to largely fabricate chiral materials, for example, asymmetric plasmonic tetramers,[8,9] Born−Kuhn model structures,[10] and loop-wire metaatoms,[11] etc. A large collection of chiral plasmonic "molecules" including gold nanoparticle (AuNP) dimers,[12,13] tetramers,[14] pyramids,[15,16] and gold nanorod (AuNR) dimers[17,18] have been reported using DNA or protein guided self-assembly. Recently, chiral plasmonic superstructures such as AuNP helices[19−23] were introduced based on peptide, DNA origami, or supramolecular nanofiber templates. Besides, by adsorbing AuNRs on twisted fibers or incorporating AuNRs into cellulose nanocrystal films, chiroptical activities were also found from these resulted nanocomposites.[24,25] However, aside from these discoveries, more sophisticated chiral structures with defined geometry and enhanced optical activities are still needed, as new insights into the controllable creation of nanostructural chirality are discovered and applications of chiral structures continue to be expanded.[26,27]

Three-dimensional (3D) chiral superstructures that have precise 3D ordering of nanomaterials and intentionally introduced asymmetry can display far more morphological and structural complexity and even advanced functionalities. By organizing anisotropic nanocrystals such as AuNRs into 3D asymmetric superstructures, enhanced chirality may be produced as compared to those of isotropic NP superstructures, benefiting from the high dissymmetry factor and the strong plasmon antenna effect of the building blocks.[12,13,25] Moreover, well-defined fabrication of 3D chiral superstructures made of anisotropic nanocrystals, which results in programmed configurations and customized chirality, is also of fundamental significance for the understanding and exploring of the nanostructural optical activities. However, this remains a great challenge as a result of the difficulties in controlled and flexible positioning, separating and rotating of anisotropic nanocrystals into a large entity with long-range order and nanoscale precision. At present, mostly studied chiral superstructures consisting of anisotropic nanocrystals possess high degree of arrangement disorder of the building blocks,[3,24,25,28,29] let alone the flexibility in tailoring the spatial parameters, such as the interparticle gap and angle. Although various strategies
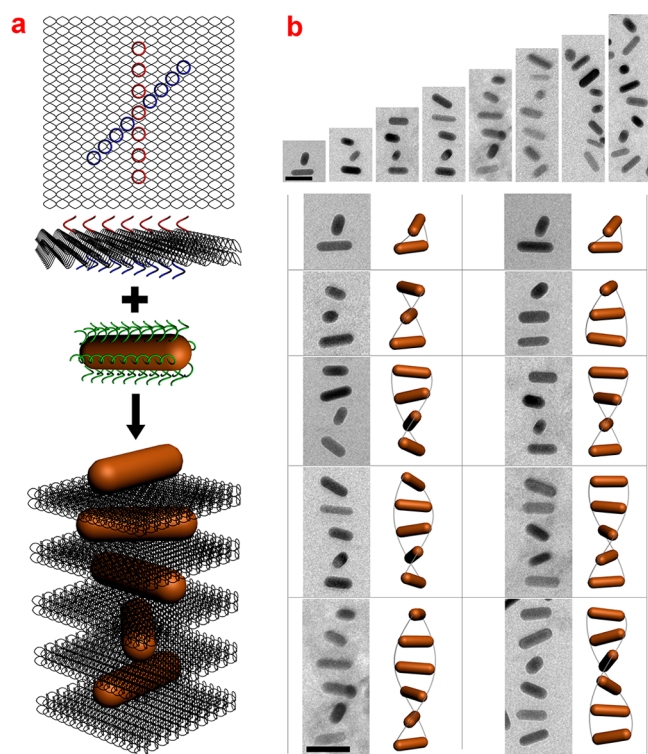
including the surface ligand interactions and the intrinsic shape-oriented attachment have been employed to arrange anisotropic building blocks, these problems have not been well resolved.[30−32]

Here, we successfully realized anisotropic AuNR helical superstructures with designed configurations including precise inter-rod spacing of 14 nm, inter-rod angle of 45°, and deterministic handedness in a simple fashion. In principal, DNA capturing strands were predesigned on the opposite sides of a 2D origami template and form a centrosymmetric 'X' shape, so that AuNRs modified with the complementary DNA sequences were bound onto the 2D DNA origami, stacked along the normal direction and rotated around the normal direction. As a proof of concept, two types of optically reversed AuNR helices were self-assembled under the guidance of DNA origami with fixed inter-rod spacing of 14 nm and inter-rod angle of 45°, by solely designing the mirrored-symmetric patterns of capturing strands on the origami. Circular dichroism (CD) spectra measurement showed that the assembled AuNR helices display strong and predicted chiroptical activities, which match well with the calculated results.
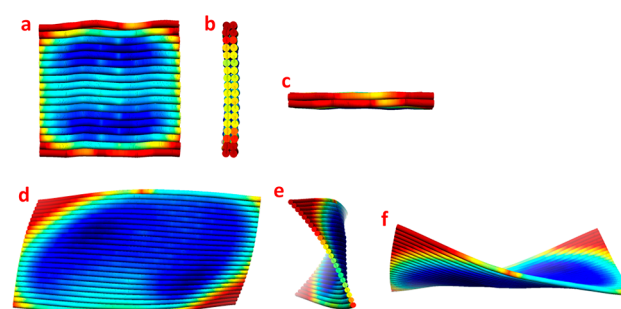
Figure 1a schematically illustrates the strategy for self-assembly of AuNR helices templated by DNA origami. For explanatory purposes, here we only presented the assembly

procedure of right-handed (RH) AuNR helices with a 45° angle between two neighboring NRs. In this case, one cycle of helix would consist of 9 AuNRs. A 2D origami (45 × 45 × 4 nm) was employed as template (Figures S1−3). The capturing strands (poly A_{15}) were arranged into a straight line on each side of the DNA origami, forming an 'X' pattern with an angle of 45°. Then, via an one-pot self-assembly procedure, the AuNRs (12 × 40 nm) modified with the complementary DNA sequences hybridized with the DNA origami, generating an AuNR-origami alternating structure in which AuNRs rotate in RH direction (Figure 1a). It is worth noting that the DNA origami can adapt different deposition in the superstructure because the capturing strands on either side of the origami can bind to a AuNR, but the spatial arrangement of AuNRs will not be affected as a result of the centrosymmetric 'X' pattern of capturing strands and the AuNR helices keep the RH-configuration. Furthermore, the handedness of the AuNR helices can be reversed by changing the pattern of capturing strands, for instances, an 'X' pattern of capturing strands with rotation angle of −45° will induce the opposite rotation of AuNRs and the formation of LH helices (Figure S2).

Cryo-transmission electron microscopy (Cryo-TEM) was used to characterize the assembled 3D AuNR helices, where the helices were frozen in the ice and preserved their 3D native geometry. Figure 1b shows the Cryo-TEM images of the obtained RH-AuNR helices with different number of AuNRs. The random orientation of AuNR helices in the ice leads to deviated 2D projections. We reconstructed the observed objects by rotating the 3D models with the same parameters as designed, AuNR of 12 × 40 nm, inter-rod distance of 14 nm, and inter-rod angle of 45°. Apparently, the observed AuNR helices match very well with the 3D model structures with corresponding orientations, unambiguously demonstrating the success of our strategy for fabricating the AuNR helical superstructures. The 3D conformation of AuNR helices keeps well when the number of AuNRs in the helices is <7. This high degree of geometrical order benefits from the excellent rigidity of the origami template. As depicted in Figure 2, the bilayer 2D


Figure 1. (a) Schematic illustration of the self-assembly of RH-AuNR helices. The capturing strands in red and blue on two opposite sides of the origami form an 'X' shape of 45°, which are shown from the top and side views of the template. All the capturing strands have the same sequence of poly A_{15}. The strands in green on AuNR surface are complementary to the capturing strands. This design enables one-pot assembly of AuNR helices. Rotation of the intermediate origami may happen as each side of the origami can bind to AuNRs, but the handedness of the helices stays unchanged. (b) Cryo-TEM images of the assembled AuNR helices with varying number of AuNRs. The reconstructed models match very well with the observed objects, demonstrating the success of the strategy. The scale bar is 50 nm.

Figure 2. Models of our bilayer origami (45 × 45 × 4 nm) and the classic rectangular origami (90 × 60 × 2 nm):[33] (a and d) front; (b and e) left side; and (c and f) top view, respectively. These models were replotted from Cando software.

origami designed in this study shows much less structural distortion as compared with the classic rectangular origami.[33] However, deviation from the designed helices may occur with further increase in the number of AuNRs, as a result of the flexibility of the capturing strands. As shown from the helices with 9 AuNRs in Figure 1b, the axis possibly turns to be a 3D curve rather than a straight line. To further verify the inter-rod distance in the AuNR helices, we also prepared parallel AuNR

superstructures, in which AuNRs are organized side-by-side. Cryo-TEM images (Figure S4) of the parallel superstructure show that the AuNRs were separated from each other with a distance close to the predesigned spacing of 14 nm. Also, uranyl acetate stained TEM images clearly show the existence of the origami template between neighboring AuNRs.

Importantly, the handedness of the AuNR helices can be rationally tailored by simply changing the pattern of capturing strands on the origami. When we modified the 'X' pattern of capturing strands into a mirrored-symmetric 'X' pattern by changing the rotation angle from 45° to −45°, the AuNRs on the DNA origami rotate toward the opposite direction, resulting in the reversal from RH-AuNR helices to LH-AuNR helices. The TEM images in Figure 3 clearly verify the
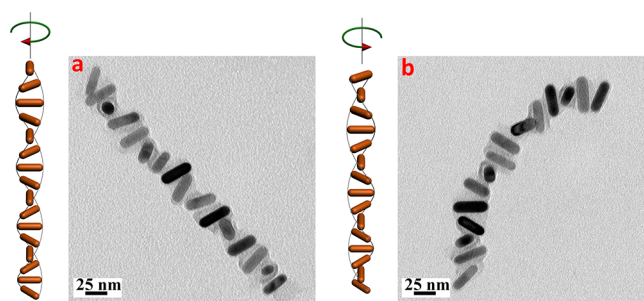
Figure 3. Models and TEM images of (a) RH-AuNR and (b) LH-AuNR helices, respectively. Uranyl acetate staining was performed during TEM sampling in order to clearly observe the DNA origami.

fabrication of both the RH- and LH-AuNR helices. By hybridizing 21 μL of purified origami (3 nM) with 5.1 μL of AuNRs (13.5 nM) following an optimized annealing process (see Experimental Section in the Supporting Information for details), RH- and LH-AuNR helices containing approximate number of AuNRs were obtained, respectively (Figure 3a,b). We must note that, due to the drying process and the 2D projection of TEM images, the AuNR helices were distorted, but the configuration of RH- and LH-AuNR helices can still be discriminated. As shown in the high-magnification TEM images in Figures 3 and S5, the different orientations of the AuNRs in the 2D images are highly related to their 3D configurations in RH- and LH-AuNR helices, respectively. The stained DNA origamis were clearly seen between neighboring AuNRs, further demonstrating that the AuNR helices were assembled under the guidance of origami template, instead of spontaneous aggregation during sampling.

Besides tuning of the handedness of AuNR helices, we further modified the number of AuNRs in the helices, that is, the length of the AuNR helices. As shown in the statistics in Figure 4, which are obtained by counting about 100 pieces from the TEM images of each sample, the peaked number of AuNRs in the assembled products decreases from 9 to 4 and 2 with increasing the AuNR/origami ratio from 1.1 to 1.7 and 2.5 in the assembly system. It is apparent that, when the AuNRs are excessive, most of the capturing strands on both sides of the origami were covered by AuNRs, leaving very few of binding sites on the origami for the continuous stacking of AuNRs. Thus, under the condition of AuNR/origami ratio of 2.5, most of the stacked structures comprising only two AuNRs were prepared. In contrast, when decreasing the amount of AuNRs close to the origami, the AuNRs can bind to capturing strands on each side of the origami continuously due to sufficient
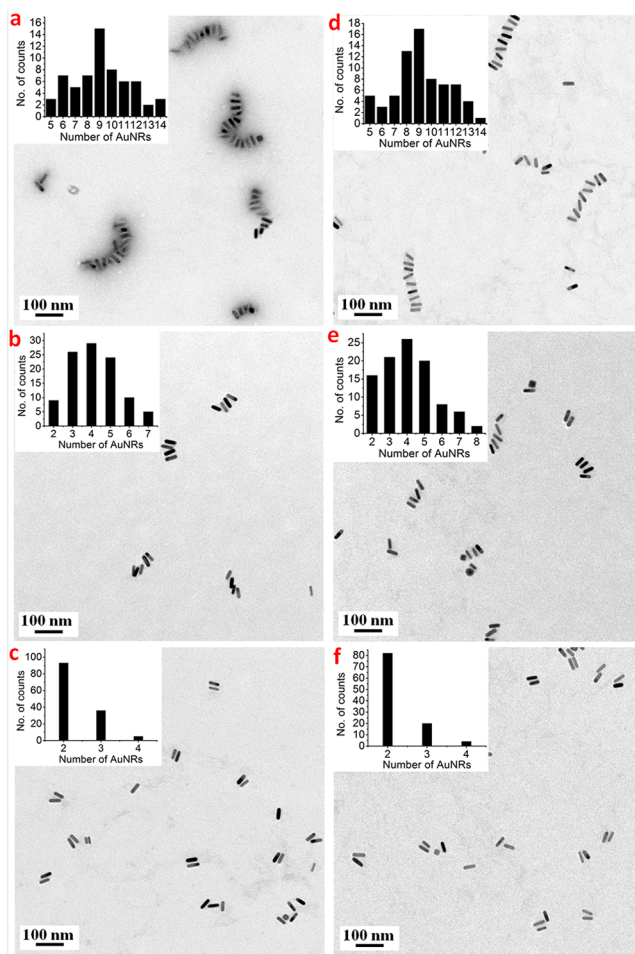
Figure 4. TEM images of (a–c) RH and (d–f) LH AuNR helices principally containing 9, 4, and 2 AuNRs, respectively, which were fabricated by varying the AuNR/origami ratio from 1.1 to 1.7 and 2.5. Insets are the statistics of the helices.

binding sites. As a result, larger degree of polymerization of AuNRs and origamis is achieved, generating longer AuNR helices. In the case of AuNR/origami ratio of 1.1, 9 AuNRs were observed in most of the assembled helices. However, because charge repulsions between AuNRs and origamis become stronger with increasing the number of AuNRs and origamis in the assembled helices, the maximum length of the helices is limited, and the longest AuNR helices in our experiments were found possessing about 20 AuNRs (Figures 3 and S5).

The dynamics of the self-assembly of AuNR helices can be simplified to that of the linear step-growth polymerization reaction, in which the origami and DNA-modified AuNRs act as two bifunctional monomers, respectively. The changing trend of the average number of AuNR in the assembled helices with the origami/AuNR molar ratio can be simply understood based on a modified Carothers equation as follows:[34]

$$N = \lambda(1 + r)/(1 + r - 2rp)$$

Where N is the average number of AuNR in the assembled helices, λ is an adjustable coefficient, r is the origami/AuNR molar ratio, and p is the extent of reaction (or the conversion of origamis assembled into AuNR helices). Based on the above modified Carothers equation, larger N is obtained when $r = 1$ and keeping λ and p constant, that is, the helix superstructures

containing more AuNRs should be assembled when the ratio of origami to AuNR is close to 1 in the self-assembling reaction, which is consistent with our experimental results.

Lastly, we systematically investigated the optical properties of the assembled RH- and LH-AuNR helices. The absorption spectra are shown in Figure S6. All of the RH- and LH-AuNR helices that principally have 9, 4, and 2 AuNRs exhibit close surface plasmon resonance (SPR) frequency as compared to single AuNR, because very weak SPR coupling arises between AuNRs that are separated with a large distance of ∼14 nm along the transverse axis. CD results (Figure 5) evidently depict the dependence of optical activities of the AuNR helices on the 3D configuration and the number of AuNR in the helices. The RH-AuNR helix produces a CD signal with a characteristic bisignate dip-peak shape, and stronger chirality was observed for the larger AuNR helices, while LH-AuNR helix generates a mirror-symmetric peak-dip CD signal with tunable CD
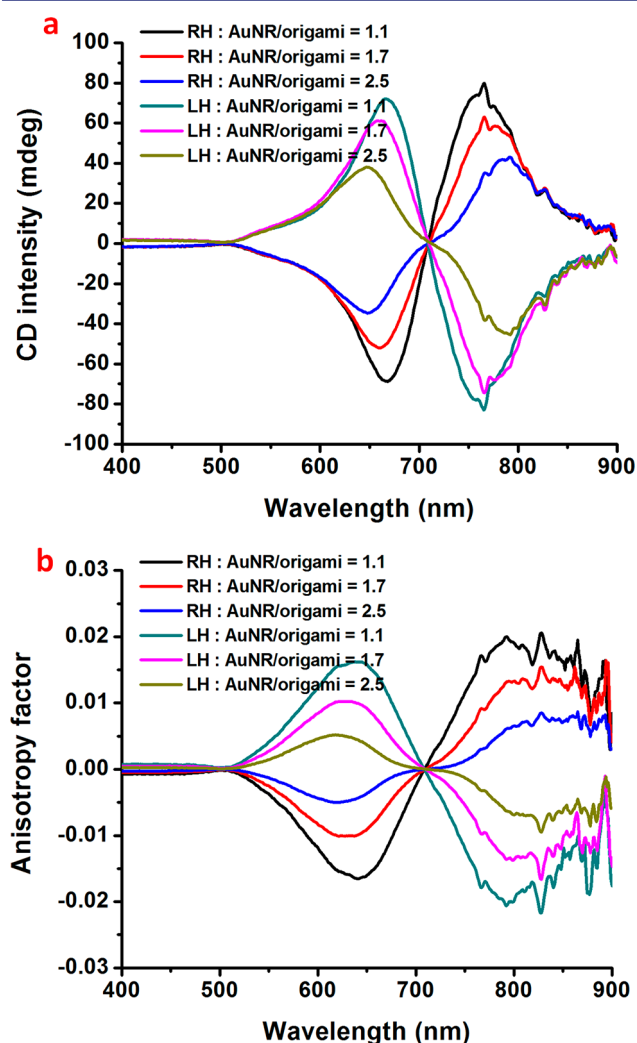
Figure 5. Experimental results of the CD spectra and anisotropy factors of AuNR helices. (a) The measured CD spectra of RH- and LH-AuNR helices containing varying numbers of AuNRs. With the AuNR/origami ratio increasing from 1.1 to 1.7 and 2.5, the statistical number of AuNRs in the resulting superstructures decreases from 9 to 4 and 2, respectively. The CD intensity is normalized according to the concentration of origamis in the assembly system. (b) The measured anisotropy factors of RH- and LH- AuNR helices corresponding to the structures in (a).

intensity. In Figure 5a, the CD spectra of all the RH- and LH-AuNR helices are normalized based on the concentration of origami. This means that the concentration of the assemblies that principally have 9 AuNRs is much lower than that of the two other smaller AuNR helices containing 4 and 2 AuNRs. However, the CD signal of the 9 AuNR helices is higher, which demonstrates that the chiroptical activities of AuNR helices can be greatly intensified by increasing the number of AuNR in the superstructures. In addition, in situ CD measurement was performed to monitor the change of CD signals of AuNR helices with assembling time. As shown in Figure S7, the results demonstrate that the AuNR helices were successfully assembled in a short time of 20 min, and also the optical activities of AuNR helices were greatly modified by changing the AuNR/origami molar ratio in the assembling reaction which decides the length of the resultant AuNR helices.

Previous studies pointed out that the helical geometry of nanoparticle assemblies show the strongest CD signals among various nanoparticle chiral structures.[35] This is because chiral collective excitation of nanoparticles can be induced from the helical geometry under external circularly polarized illumination. Similar mechanism can be applied to the AuNR helical superstructures, where the helical external field can excite the chiral collective dipole resonance of AuNRs. Thus, the helical geometry plays an elementary role in the chiral response of our AuNR superstructures. Besides, the strong plasmonic dipole resonance of AuNRs can lead to large absorption of incident electromagnetic waves (antenna effect) and increase the CD signal of the AuNR helices.

From another perspective, the optical activities of chiral structures are strongly dependent on their structural asymmetry.[16,35] The chiral response of the AuNR helices can be characterized by the dissymmetry or anisotropy factor (g-factor), defined as

$$g = \frac{\Delta\varepsilon}{\varepsilon}$$

where $\Delta\varepsilon$ and ε are the molar CD and molar extinction, respectively. As shown from Figure 5b, the anisotropy factors of RH- and LH-AuNR helices increase with increasing the length of helices. This is consistent with the measured CD signals which are enhanced by increasing the length of helices. Unexpectedly, we obtained the maximum g-factor (g_{max}) of ∼0.02 around the peak for RH-AuNR helices consisting of 9 AuNRs, and ∼ −0.02 around the dip for LH-AuNR helices consisting of 9 AuNRs. Our measured g-factors are comparable with the reported macroscopic AuNR assemblies, which show intense optical activity but have a high degree of arrangement disorder.[25] Also, for the AuNR helices, less AuNRs are necessary to generate the same g-factor as that of the macroscopic structures. It can be concluded that, the large g-factors of the AuNR helices are mainly caused by the well-controlled asymmetric helical configurations, aside from the contribution of weak plasmon coupling among AuNRs.

To gain more insights into the mechanism behind the observed chiroptical response, two numerical approaches, Scuff-EM[36,37] and a finite-element EM method (COMSOL multiphysics), were employed to obtain the extinction spectra of the assembled AuNR helices and to calculate the surface charge distribution profiles of the AuNRs in the helices, respectively. In these calculations, the AuNRs were modeled as a cylinder with two hemispherical caps at both ends. For simplicity, only the situation that the circularly polarized light (CPL)

propagates on the direction of the helical axis of the AuNR helices was considered.

Figure 6a shows calculated CD extinction spectra of the assembled AuNR helices consisting of 2, 4, and 9 AuNRs,
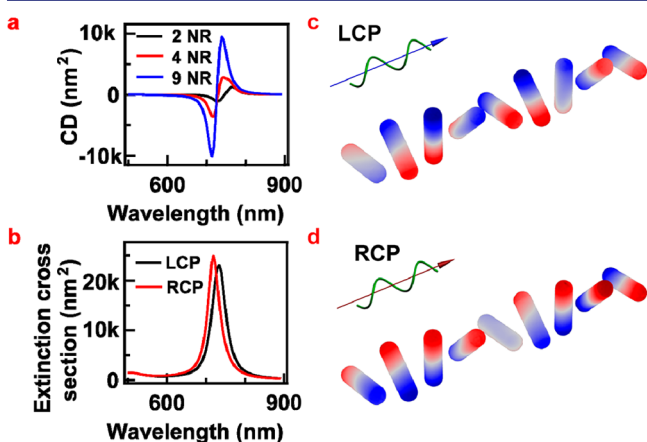
Figure 6. Calculated chiroptical response of the AuNR helices. (a) CD extinction spectra of RH-AuNR helices consisting of 2, 4, and 9 AuNRs, respectively. (b) Extinction cross section of the RH-AuNR helices consisting of 9 AuNRs under the excitation of incident light with LCP (black) and RCP (red). (c and d) LCP and RCP induced surface charge distribution profile.

respectively. When the number of AuNR in the helices is increased, the dip to peak intensity of the spectrum increases. The intensity increase is found consistent with the experimental observations (Figure 5a). These chiroptical responses of the AuNR helical superstructures can be readily understood. As a chiral object, the incident circularly polarized light possesses electric field with a helical spatial distribution of left or right handedness. Such a spatially distributed helical electric field can intensely interact with the AuNR helix by exciting a collective plasmonic mode. As incident light with left and right circular polarization (LCP and RCP) possess opposite helical arrangements of electric field, different collective plasmon modes are excited, and hence distinct chiroptical responses are observed. For example, under the excitation of light with RCP, the AuNR helices consisting of 9 AuNRs exhibit a single plasmonic resonance at 720 nm in the extinction spectrum (Figure 6b). This resonance is shifted to 740 nm when an opposite excitation of light with LCP is applied.

Figure 6c,d depicts the simulated surface charge distribution profiles of the RH-AuNR helices consisting of 9 AuNRs under LCP and RCP excitation, respectively, which further help to understand the collective oscillation modes of the surface plasmons. It shows that under the excitation of the helical external field, most of the AuNRs behave as electric dipoles with the directions oriented along their long axes. Thus, the plasmon resonance energy is mainly affected by the oscillation modes of the neighboring dipoles. For example, paralleled oscillation increases the resonance energy, while the antiparalleled one decreases it. As shown in Figure 6c,d, for LCP, the quasi-paralleled charge distribution configuration reproduces three by three AuNRs, with the fourth deviated from the handedness, while for RCP, the number is five. Therefore, RCP excites a blue-shifted resonance compared to LCP (Figure 6b). As a result, by subtracting RCP from LCP, the CD spectra exhibit a characteristic dip-peak bisignated line shape (Figure 6a). Similar discussion can be applied to the LH-AuNR helical

superstructures, where inversed CD spectra are reasonably expected.

In conclusion, by using anisotropic AuNRs as building blocks, we realized AuNR helical superstructures with right- and left-handedness, respectively, in a facile and programmable manner. Strong plasmonic chiral responses of the AuNR helices consistent with the handedness were observed. The number of AuNRs contained in helices was also tailored by varying the origami/AuNR molar ratio in the self-assembly system, and thus the resulted chiral signal intensity was delicately tuned. The optical activities of the AuNR helices will be further investigated by changing the inter-rod angle and distance in future experiments. Above all, our study provides a novel strategy for 3D self-assembly of anisotropic nanomaterials with both long-range order and nanoscale precision. Moreover, by exploring the high addressability of origami template for positioning of fluorescent dyes or quantum dots, fluorescence combined chiral materials or broad band chiral materials with designed optical properties can be promisingly realized. Also, the anisotropic helical superstructures could be potentially developed as chiral fluids for future sensing or negative index materials, benefiting from their giant plasmonic chirality.

■ ASSOCIATED CONTENT

Ⓢ Supporting Information

Experimental details, more TEM images and DNA sequences. This material is available free of charge via the Internet at http://pubs.acs.org.

■ AUTHOR INFORMATION

Corresponding Author

qbwang2008@sinano.ac.cn

Notes

The authors declare no competing financial interest.

■ ACKNOWLEDGMENTS

■ REFERENCES

(1) Zhu, Z.; Guo, J.; Liu, W.; Li, Z.; Han, B.; Zhang, W.; Tang, Z. *Angew. Chem., Int. Ed.* **2013**, *125*, 13816.

(2) Hendry, E.; Carpy, T.; Johnston, J.; Popland, M.; Mikhaylovskiy, R. V.; Lapthorn, A. J.; Kelly, S. M.; Barron, L. D.; Gadegaard, N.; Kadodwala, M. *Nat. Nanotechnol.* **2010**, *5*, 783.

(3) Li, Z.; Zhu, Z.; Liu, W.; Zhou, Y.; Han, B.; Gan, Y.; Tang, Z. *J. Am. Chem. Soc.* **2012**, *134*, 3322.

(4) Lan, X.; Wang, Q. *NPG Asia Mater.* **2014**, *6*, e97; 10.1038/am.2014.16.

(5) Shopsowitz, K. E.; Qi, H.; Hamad, W. Y.; MacLachlan, M. J. *Nature* **2010**, *468*, 422.

(6) Pendry, J. B. *Science* **2004**, *306*, 1353.

(7) Abdulrahman, N. A.; Fan, Z.; Tonooka, T.; Kelly, S. M.; Gadegaard, N.; Hendry, E.; Govorov, A. O.; Kadodwala, M. *Nano Lett.* **2012**, *12*, 977.

(8) Hentschel, M.; Schäferling, M.; Weiss, T.; Liu, N.; Giessen, H. *Nano Lett.* **2012**, *12*, 2542.

(9) Hentschel, M.; Wu, L.; Schäferling, M.; Bai, P.; Li, E. P.; Giessen, H. *ACS Nano* **2012**, *6*, 10355.

(10) Yin, X.; Schäferling, M.; Metzger, B.; Giessen, H. *Nano Lett.* **2013**, *13*, 6238.

(11) Helgert, C.; Pshenay-Severin, E.; Falkner, M.; Menzel, C.; Rockstuhl, C.; Kley, E.-B.; Tünnermann, A.; Lederer, F.; Pertsch, T. *Nano Lett.* **2011**, *11*, 4400.

(12) Wu, X.; Xu, L.; Liu, L.; Ma, W.; Yin, H.; Kuang, H.; Wang, L.; Xu, C.; Kotov, N. A. *J. Am. Chem. Soc.* **2013**, *135*, 18629.

(13) Zhao, Y.; Xu, L.; Ma, W.; Wang, L.; Kuang, H.; Xu, C.; Kotov, N. A. *Nano Lett.* **2014**, *14*, 3908.

(14) Shen, X.; Asenjo-Garcia, A.; Liu, Q.; Jiang, Q.; Javier García de Abajo, F.; Liu, N.; Ding, B. *Nano Lett.* **2013**, *13*, 2128.

(15) Mastroianni, A. J.; Claridge, S. A.; Alivisatos, A. P. *J. Am. Chem. Soc.* **2009**, *131*, 8455.

(16) Yan, W.; Xu, L.; Xu, C.; Ma, W.; Kuang, H.; Wang, L.; Kotov, N. A. *J. Am. Chem. Soc.* **2012**, *134*, 15114.

(17) Ma, W.; Kuang, H.; Wang, L.; Xu, L.; Chang, W.; Zhang, H.; Sun, M.; Zhu, Y.; Zhao, Y.; Liu, L.; Xu, C.; Link, S.; Kotov, N. A. *Sci. Reports* **2013**, *3*, 1934.

(18) Lan, X.; Chen, Z.; Dai, G.; Lu, X.; Ni, W.; Wang, Q. *J. Am. Chem. Soc.* **2013**, *135*, 11441.

(19) Kuzyk, A.; Schreiber, R.; Fan, Z.; Pardatscher, G.; Roller, E.; Högele, A.; Simmel, F. C.; Govorov, A. O.; Liedl, T. *Nature* **2012**, *483*, 311.

(20) Shen, X.; Song, C.; Wang, J.; Shi, D.; Wang, Z.; Liu, N.; Ding, B. *J. Am. Chem. Soc.* **2012**, *134*, 146.

(21) Jung, S. H.; Jeon, J.; Kim, H.; Jaworski, J.; Jung, J. H. *J. Am. Chem. Soc.* **2014**, *136*, 6446.

(22) Song, C.; Blaber, M. G.; Zhao, G.; Zhang, P.; Fry, H. C.; Schatz, G. C.; Rosi, N. L. *Nano Lett.* **2013**, *13*, 3256.

(23) Sharma, J.; Chhabra, R.; Cheng, A.; Brownell, J.; Liu, Y.; Yan, H. *Science* **2009**, *323*, 112.

(24) Querejeta-Fernández, A.; Chauve, G.; Methot, M.; Bouchard, J.; Kumacheva, E. *J. Am. Chem. Soc.* **2014**, *136*, 4788.

(25) Guerrero-Martínez, A.; Auguié, B.; Alonso-Gómez, J. L.; Džolić, Z.; Gómez-Graña, S.; Žinić, M.; Cid, M. M.; Liz-Marzán, L. M. *Angew. Chem., Int. Ed.* **2011**, *123*, 5613.

(26) Wang, Y.; Xu, J.; Wang, Y.; Chen, H. *Chem. Soc. Rev.* **2013**, *42*, 2930.

(27) Wang, Y.; Wang, Q.; Sun, H.; Zhang, W.; Chen, G.; Wang, Y.; Shen, X.; Han, Y.; Lu, X.; Chen, H. *J. Am. Chem. Soc.* **2011**, *133*, 20060.

(28) Zhu, Z.; Liu, W.; Li, Z.; Han, B.; Zhou, Y.; Gao, Y.; Tang, Z. *ACS Nano* **2012**, *6*, 2326.

(29) Wang, R.-Y.; Wang, H.; Wu, X.; Ji, Y.; Wang, P.; Tai-Shung Chung, Y. Q. *Soft Matter.* **2011**, *7*, 8370.

(30) Liu, K.; Nie, Z.; Zhao, N.; Li, W.; Rubinstein, M.; Kumacheva, E. *Science* **2010**, *329*, 197.

(31) Miszta, K.; Graaf, J.; Bertoni, G.; Dorfs, D.; Brescia, R.; Marras, S.; Ceseracciu, L.; Cingolani, R.; Roij, R.; Dijkstra, M.; Manna, L. *Nat. Mater.* **2011**, *10*, 872.

(32) Jones, M. R.; Macfarlane, R. J.; Lee, B.; Zhang, J.; Young, K. L.; Senesi, A. J.; Mirkin, C. A. *Nat. Mater.* **2010**, *9*, 913.

(33) Ke, Y.; Lindsay, S.; Chang, Y.; Liu, Y.; Yan, H. *Science* **2008**, *319*, 180.

(34) Allcock, H. R.; Lampe, F. W.; Mark, J. E. *Contemporary Polymer Chemistry*, 3rd ed.; Prentice Hall: Upper Saddle River, NJ, 2003.

(35) Fan, Z.; Govorov, A. O. *Nano Lett.* **2010**, *10*, 2580.

(36) Homer Reid, M. T.; Johnson, S. G. *ArXiv e-prints* **2013**, *1307*, 2966.

(37) *SCUFF-EM*; M. T. Homer Reid, MIT: Cambridge, MA, 2013; http://homerreid.com/scuff-EM.